Asymptotic softness of a laterally confined sheet in a pressurized chamber

Oz Oshri*

Department of Mechanical Engineering, Ben-Gurion University of the Negev, Beer-Sheva 84105, Israel

(Received 4 July 2021; accepted 18 October 2021; published 18 November 2021)

Elastohydrodynamic models, that describe the interaction between a thin sheet and a fluid medium, have been proven successful in explaining the complex behavior of biological systems and artificial materials. Motivated by these applications we study the quasistatic deformation of a thin sheet that is confined between the two sides of a closed chamber. The two parts of the chamber, above and below the sheet, are filled with an ideal gas. We show that the system is governed by two dimensionless parameters, Δ and η, that account respectively for the lateral compression of the sheet and the ratio between the amount of fluid filling each part of the chamber and the bending stiffness of the sheet. When $\eta \ll 1$ the bending energy of the sheet dominates the system, the pressure drop between the two sides of the chamber increases, and the sheet exhibits a symmetric configuration. When $\eta \gg 1$ the energy of the fluid dominates the system, the pressure drop vanishes, and the sheet exhibits an asymmetric configuration. The transition between these two limiting scenarios is governed by a third branch of solutions that is characterized by a rapid decrease of the pressure drop. Notably, across the transition the energetic gap between the symmetric and asymmetric states scales as $\delta E \sim \Delta^2$. Therefore, in the limit $\Delta \ll 1$ small variations in the energy are accompanied by relatively large changes in the elastic shape.

DOI: 10.1103/PhysRevE.104.055005

I. INTRODUCTION

The interaction between thin elastic objects and fluid interfaces has attracted much attention recently, because numerous biological systems and technological applications exploit mechanical instabilities to ascertain their proper functionality [1–20]. Morphogenesis of epithelial sheets [21,22], and the growth of biofilms on soft or fluidlike substrates [23,24], are just two examples for the ways nature generates complex patterns to stabilize living systems. Similarly, elastohydrodynamic instabilities are exploited to fabricate flexible surfaces in electronic devices [25], and in the field of soft robotics [26].

Motivated by these applications we focus in this paper on the fundamental building blocks comprising the quasistatic interaction between a thin sheet and an ideal gas. Our system consists of a closed chamber that is partitioned by a thin sheet into two parts, each of which is filled with an ideal gas. Given the total length of the sheet, the dimensions of the chamber, and the amount of fluid filling each side, we investigate how the elastic configuration is correlated to the pressure drop, and consequently the volume difference, that is induced in the chamber (see further details in Fig. 1).

Our study reveals that the behavior of the system is governed by two dimensionless numbers. One is the lateral displacement, Δ, that accounts for the ratio between the total length of the sheet and the width of the chamber, and a second parameter that accounts for the ratio between the amount of fluid filling each part of the chamber and the bending stiffness of the sheet. We denote the latter parameter by η and name it the "bendo-gases" parameter.

Accordingly, we show that the state diagram of the system, spanned on the (η, Δ) plane, is governed by three different branches of solutions. When $\eta \ll 1$ the bending energy dominates the system, the pressure drop in the chamber increases, and the sheet exhibits a solution that is closed in shape to the symmetric, first mode of buckling. However, when $\eta \gg 1$ the energy of the fluid dominates the system and acts to set the volume difference, and therefore the pressure drop, to zero. As a result, this region is characterized by an asymmetric configuration of the sheet. The transition between these two limiting cases is accompanied by a third branch of solutions that allows for a continuous transition between the symmetric and asymmetric configurations. In particular, we show using a numerical analysis that the transition region emerges as a nonlinear effect; i.e., while it appears as an unstable solution at the leading order of the analysis, it becomes stable once higher nonlinear corrections are considered. The width along the η axis over which the latter branch stabilizes scales as $\sim\Delta$. Across this narrow region the energy changes by an order of $\sim\Delta^2$. Therefore, as the lateral displacement diminishes, the system becomes asymptotically softer; i.e., the sheet can undergo relatively large deformations at small energetic cost.

We conjecture that under the appropriate design our system, and its dynamic extensions, can be exploited to activate small-scale devices, such as energy harvesters and microsized pumps. For example, suppose that the elastic sheet is covered with piezoelectric patches, and that the chamber is constantly exposed to a source of an external energy, such as acoustic waves [27–29]. Then, if the natural frequency of the system is designed to match with the frequency of the external source, the oscillations of the elastic sheet can potentially supply electric power to small-scale devices. An interesting aspect within this energy harvesting application is a scenario in which the

*oshrioz@bgu.ac.il

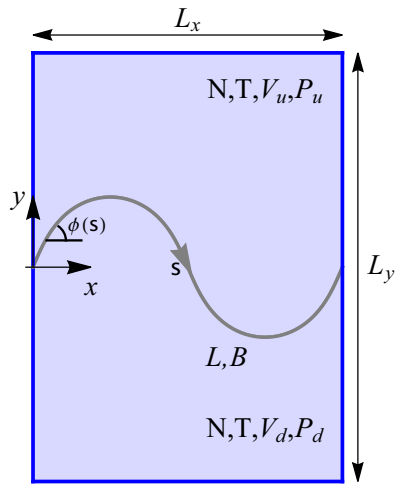

FIG. 1. Schematic overview of the system. A rectangular chamber with dimensions $L_x \times L_y$ is divided into two parts by a thin sheet that has a total length L and bending modulus B. The upper and lower parts of the chamber are filled with an ideal gas with N particles and a temperature T. At equilibrium, the volumes and the pressures in each side of the chamber are given by V_i and P_i respectively ($i = \mathrm{u}, \mathrm{d}$). A Cartesian coordinate system is located on the left edge of the sheet. The elastic configuration is determined by the tangent angle, $\phi(s)$, where s is the arc-length parameter.

system is designed to operate close to the transition region, where the sheet becomes very soft. In this case, the sheet may undergo large deformations, and therefore increase its efficiency, even if the intensity of the external source is rather small. Note that while the complete analysis of this dynamical system requires to include inertial effects in the analytical model, the quasistatic solution obtained herein provides us, on the one hand, with the base solution around which these dynamic extensions are expanded and, on the other hand, with a specific region in the parameter space where this application can be most efficient.

Another example for a potential applicability of the system is in the design of micropumps. These pumps are used, for example, to deliver individual microsized particles through microchannels or to move very small volumes of liquids [30,31]. In our system, pumping can be realized in the following way. When the two parts of the chamber are filled with a fluid the system essentially stores energy due to the deviations of the sheet from the lowest mode of buckling and the pressure difference that these deviations induce in the chamber. This stored energy can be exploited, for example, when fluid is allowed to exchange between the two sides of the chamber (see a prototypical model of this system in Ref. [32]). In this case, the fluid's dynamics will act to set the pressure difference in the chamber to zero, and the sheet will act to restore the first mode of buckling. This dynamic process, if appropriately managed, can be tuned to create very small bursts of pressure drops that potentially can pump individual small particles.

The paper is organized as follows. In Sec. II we formulate the problem, derive the equilibrium equations, and discuss the schematic evolution of the system. In Sec. III we expand the equilibrium equations in the small amplitude approximation, derive their corresponding solutions, and discuss the transitions between different branches of solutions. In Sec. IV we compare the leading order analysis with the numerical solution of the nonlinear equations, and highlight the differences between them. In addition, we derive the properties of the transition region, and provide an estimation for the pressure drop throughout the evolution of the system. In Sec. V we conclude, summarize our main results, and discuss possible extensions for future studies.

II. FORMULATION OF THE PROBLEM

An inextensible thin sheet with total length L and bending modulus B is compressed symmetrically against the two sides of a rectangular closed chamber (see Fig. 1). The horizontal, the vertical, and the width dimensions of the chamber are denoted by L_x, L_y, and W, respectively. A Cartesian coordinate system is located on the left edge of the sheet. We assume that the sheet can only deform in the xy plane, and therefore set $W = 1$. The volumes of the chamber above and below the elastic sheet, V_u and V_d, are filled with the same amount of an ideal gas, where hereafter subscripts "u" and "d" correspond to fields that are calculated respectively above and below the elastic sheet. The ideal gas satisfies the equation of state,

$$P_i V_i = N k_\mathrm{B} T, \tag{1}$$

where $i = \mathrm{u}, \mathrm{d}$, P_i are the upper and lower pressures, N is the number of particles, k_B is the Boltzmann constant, and T is the temperature. The system is assumed to be in contact with a thermal bath, and therefore the temperature remains constant at all times. In addition, we assume that the volume occupied by the elastic sheet is negligible compared with the volume of the sheet, i.e., $tL/L_xL_y \ll 1$, where t is the sheet's thickness. Therefore, we have that $V_\mathrm{d} + V_\mathrm{u} = L_xL_y$.

Given the physical parameters of the sheet, L and B, the dimensions of the chamber, L_x and L_y, and the amount of fluid filling each part of the chamber, $Nk_\mathrm{B}T$, we look for the corresponding shape of the elastic sheet, and the pressure difference between the two sides of the chamber; i.e., $P_\mathrm{ud} \equiv P_\mathrm{u} - P_\mathrm{d}$.

To do that, we first note that the configuration of the sheet on the xy plane, $\mathbf{x} = [x(s), y(s)]$, is given by

$$x(s) = \int_0^s \cos\phi(s')ds', \tag{2a}$$

$$y(s) = \int_0^s \sin\phi(s')ds', \tag{2b}$$

where $\phi(s)$ is the tangent angle between the sheet and the x axis, and $s \in [0, L]$ is the arc-length parameter. Second, we use this position vector to write the total energy of the system. This energy comprises of two main contributions: one is the elastic energy of the sheet, E_b, and the second is the energy of the ideal gases, E_g. Therefore, the total energy is given by

$$E = \frac{B}{2}\int_0^L \dot{\phi}^2 ds - Nk_\mathrm{B}T \ln V_\mathrm{u} - Nk_\mathrm{B}T \ln V_\mathrm{d}, \tag{3}$$

where $\dot{()} = d/ds$. While the first term in the right-hand side of Eq. (3) accounts for the bending energy of the sheet, the second and third terms account for the Helmholtz free ener-

gies of the fluids. The latter energies are presented up to some additional constants that do not depend on the sheet's configuration, and therefore only shift the energy by a constant. Following Ref. [32] we can relate the volumes of the fluid to the elastic configuration by

$$V_i = \frac{1}{2}\int_0^L \mathbf{x}\cdot\hat{\mathbf{n}}_i ds + \frac{L_x L_y}{2}, \tag{4}$$

where $\hat{\mathbf{n}}_i = \pm(-\sin\phi, \cos\phi)$ is an outwards normal vector to the enclosed area.

The equilibrium configurations of the system are determined by minimization of the total energy, Eq. (3), given the constraints, Eqs. (2). In order to derive these equations we first normalize all lengths in our system by the relaxed length of the sheet L (say, $s \to s/L$, etc.), and the total energy by B/L [$E \to E/(B/L)$]. Second, we modify the energy in Eq. (3) to account for the geometric constraints. This gives

$$G = \int_0^1 \left[\frac{1}{2}\dot{\phi}^2 - Q_x(s)(\dot{x} - \cos\phi) - Q_y(s)(\dot{y} - \sin\phi)\right] ds - \eta(\ln V_\mathrm{u} + \ln V_\mathrm{d}), \tag{5}$$

where $Q_x(s)$ and $Q_y(s)$ are two Lagrange multipliers that account respectively for the geometric constraints, Eqs. (2a) and (2b). In addition, we define the parameter

$$\eta \equiv \frac{N k_\mathrm{B} T}{B/L}, \tag{6}$$

that expresses the amount of fluid filling each part of the chamber, relative to the bending stiffness of the sheet. Hereafter we name this constant the "bendo-gases" parameter [33].

Third, we minimize Eq. (5) with respect to $\{\phi, x, y, Q_x, Q_y\}$. This gives the following equilibrium equations:

$$\ddot{\phi} + \frac{P_\mathrm{ud}}{2}(x\cos\phi + y\sin\phi) + Q_x\sin\phi - Q_y\cos\phi = 0, \tag{7a}$$

$$\dot{x} - \cos\phi = 0, \tag{7b}$$

$$\dot{y} - \sin\phi = 0, \tag{7c}$$

$$\dot{Q}_x - \frac{P_\mathrm{ud}}{2}\sin\phi = 0, \tag{7d}$$

$$\dot{Q}_y + \frac{P_\mathrm{ud}}{2}\cos\phi = 0. \tag{7e}$$

Note that the parameter η appears implicitly in these equations through the pressure difference, P_ud. Indeed, using our normalization convention, we have from Eq. (1) that

$$P_\mathrm{ud} = \eta\left(\frac{1}{V_\mathrm{u}} - \frac{1}{V_\mathrm{d}}\right). \tag{8}$$

To close the system of equations the following boundary conditions are assumed:

$$x(0) = 0, \tag{9a}$$

$$x(1) = L_x \equiv 1 - \Delta, \tag{9b}$$

$$y(0) = y(1) = 0, \tag{9c}$$

$$\dot{\phi}(0) = \dot{\phi}(1) = 0, \tag{9d}$$

where we defined the normalized lateral displacement $\Delta = 1 - L_x$ in Eq. (9b), and we specialized to the case of a hinged sheet, Eq. (9d).

We can further simplify our set of equilibrium equations, Eqs. (7). To do that, we integrate Eqs. (7d) and (7e) using Eqs. (7b) and (7c). This gives $Q_x(s) = \frac{P_\mathrm{ud}}{2}y + P_x$ and $Q_y(s) = -\frac{P_\mathrm{ud}}{2}x + P_y$, where P_x and P_y are the constants of integration. Substituting the latter solutions in Eq. (7a), we obtain

$$\ddot{\phi} + P_\mathrm{ud}(x\cos\phi + y\sin\phi) + P_x\sin\phi - P_y\cos\phi = 0. \tag{10}$$

This equation describes the balance of normal forces on a finite element of the sheet. Within this balance of forces the constants P_x and P_y denote the reaction forces that the chamber applies on the sheet at $s = 0$. We note that some properties of this equation have been previously investigated (see Refs. [32,34,35] and references therein).

This completes the formulation of the problem. In summary, given the vertical dimension of the chamber, L_y, the lateral displacement, Δ, and the bendo-gases parameter η, we can determine the ultimate orientation of the sheet, i.e., the elastic fields $\phi(s)$, $x(s)$, and $y(s)$, from the simultaneous solution of Eqs. (7b), (7c), and (10). The various constants in this solution are determined from the equation of state, and the boundary conditions, Eqs. (8) and (9).

We add two comments regarding the symmetries in our model. First, the problem has a mirror symmetry around the x axis; i.e., flipping the sign of $\{y, \phi, P_y, P_\mathrm{ud}\}$ while keeping $\{x, P_x\}$ fixed does not change the equilibrium equations and the boundary conditions. Hence, without loss of generality, in the following analysis we always assume that the sheet buckles upwards such that the pressure difference remains positive, $P_\mathrm{ud} \geqslant 0$. We keep in mind that the downwards solutions, with $P_\mathrm{ud} \leqslant 0$, are obtained by a reflection of the elastic shapes around the horizontal axis. Second, the system has another symmetry for reflection around the midaxis of the chamber, $x = (1 - \Delta)/2$. Indeed, when the x coordinate of the sheet is reflected around this axis, $x \to 1 - \Delta - x(s)$, the tangent angle flips sign, $\phi \to -\phi$, the arc-length parameter is reversed, $s \to 1 - s$, and the vertical reaction force is modified into $P_y \to -P_y + P_\mathrm{ud}(1 - \Delta)$, the equations and the boundary conditions remain unchanged. We will refer to the latter symmetry in Sec. III B 2 when we analyze a branch of elastic solutions that are not symmetric around the midaxis. We note that both of these symmetries emanate from the boundary conditions, Eqs. (9c) and (9d), which are assumed similar at the two edges of the sheet.

Schematic overview of the system

The ultimate configuration of the sheet comprises from the competition between the bending energy of the sheet and the energy of the fluid [see Eq. (3)]. This competition is manifested in the bendo-gases parameter, η, that essentially defines two opposite limits of the system. On the one hand, when $\eta \ll 1$ the fluid's energy is negligible and the bending energy dominates the system's behavior. On the other hand, when $\eta \gg 1$ the bending contribution becomes negligible and the elastic configuration is dominated by the energy of the fluid.

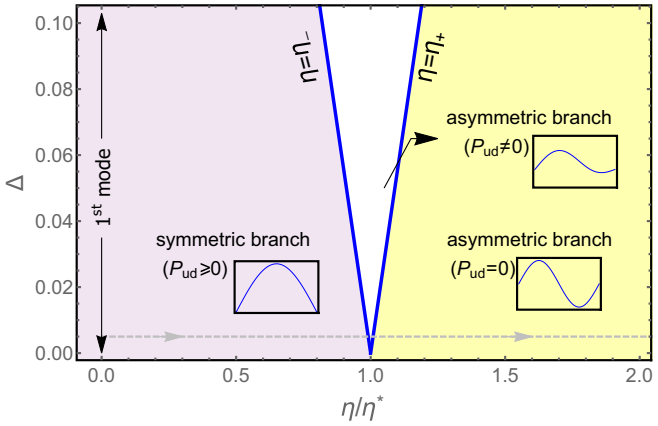

FIG. 2. The state diagram of the system on the $(\eta/\eta^\star, \Delta)$ plane, where $\eta^\star = 6\pi^4/(3+\pi^2)$. The evolution of the system is governed by three branches of solutions. A symmetric branch (light purple shaded area) governs the system when $\eta < \eta_-$. This branch is characterized by a nonzero pressure difference and symmetric configurations. In the limit $\eta \to 0$ the elastic shape converges to the first mode of buckling (see Sec. III B 1). At the transition region, $\eta_- < \eta < \eta_+$, the system is governed by a different set of solutions, which we call an asymmetric branch with $P_{\rm ud} \neq 0$ (white background). The region of stability of this branch depends on Δ, and shrinks to zero as the lateral displacement diminishes. Beyond the transition, $\eta > \eta_+$, the system is governed by the asymmetric branch with $P_{\rm ud} = 0$ (yellow shaded area). The elastic shape in this region exhibits an asymmetric profile (see Sec. III B 2). The dashed gray line indicates the direction of our numerical example in Sec. IV A.

Indeed, when η is small, we would expect the system to exhibit the first mode of buckling, that is obtained by minimization of the bending energy alone. However, when η is large and the bending contribution is negligible, minimization of the fluid's energy, $dE_g/dV_u = 0$ where $E_g = -\eta(\ln V_u + \ln V_d)$, gives $V_u = V_d$; i.e., the upper and lower sides of the chamber have equal volumes, and therefore equal pressures, at equilibrium. Obviously, the first mode of buckling, which is symmetric around the midaxis of the chamber, does not satisfy this requirement. One possible configuration that satisfies this zero volume difference condition is the second mode of buckling. Our detailed analysis indeed verifies that this is the system's minimizer.

Accordingly, the forthcoming analysis focuses on the investigation of the transition between the bending dominated and the fluid's dominated regions of the system. The main results of this investigation are presented in the "state diagram" in Fig. 2, that is plotted on the $(\eta/\eta^\star, \Delta)$ plane, where $\eta^\star$ is a critical value of the bendo-gases parameter close to which the transition occurs.

This state diagram consists of three branches of solutions. One is the symmetric branch that emerges at relatively small values of $\eta/\eta^\star$, i.e., in the bending dominated region. The elastic pattern in this branch exhibits a symmetric shape that converges to the first mode of buckling when $\eta \to 0$. The second branch dominates the transition region of the system, $\eta_- \leqslant \eta \leqslant \eta_+$, where η_- and η_+ depend on the lateral displacement, Δ. We will show that the region of stability of this branch shrinks to zero as the lateral displacement diminishes. The elastic pattern in this branch does not have a proper symmetry. The third branch corresponds to relatively large values of $\eta/\eta^\star$ and is related to the fluid's dominated region. The elastic shape in this region coincides with the second mode of buckling in the framework of Euler's elastica.

III. APPROXIMATED SOLUTIONS IN THE SMALL AMPLITUDE APPROXIMATION

In this section we derive analytical solutions to our system of equations under the assumption that the lateral displacement remains small, i.e., $\Delta \ll 1$.

Considering Eqs. (7b) and (7c), this assumption implies that the sheet's trajectory on the xy plane is given by $\dot{y} \simeq \phi$ and $\dot{x} \simeq 1 - \frac{1}{2}\dot{y}^2$. Exploiting these approximations to linearize Eq. (10) gives

$$\dddot{y} + P_x \dot{y} = -P_{\rm ud} s + P_y. \tag{11}$$

The general solution of this equation is given by

$$y(s) = a_1 + a_2 \cos(\sqrt{P_x} s) + a_3 \sin(\sqrt{P_x} s) + \frac{P_y}{P_x} s - \frac{P_{\rm ud}}{2P_x} s^2, \tag{12}$$

where a_i $(i = 1, \ldots, 3)$, P_x, P_y, and $P_{\rm ud}$ are six unknown constants that are yet to be determined by the boundary conditions, Eqs. (9b)–(9d), and the equation of state, Eq. (8). In the small amplitude approximation the latter equation reduces to

$$P_{\rm ud} = \frac{8\eta}{L_y^2} \int_0^1 y(s) ds, \tag{13}$$

where we used $V_i \simeq \frac{L_y}{2} \pm \int_0^1 y(s) ds$ $(L_x = 1 - \Delta \simeq 1)$ [see Eq. (4)]. Equation (13) indicates that our linearized solution depends on the parameter $\tilde{\eta} \equiv \eta/L_y^2$, rather than the two independent parameters, η and L_y. For this reason, in the following analysis we set $L_y = 1$ and keep in mind that, in general, η depends on the normalized vertical dimension.

In addition, our approximation implies that the lateral displacement, Eq. (9b), and the total elastic energy, Eq. (3), are related to the sheet's configuration by

$$\Delta = \frac{1}{2} \int_0^1 \dot{y}^2 ds, \tag{14a}$$

$$E - E_0 = \frac{1}{2} \int_0^1 \ddot{y}^2 ds + 4\eta \left(\int_0^1 y ds \right)^2, \tag{14b}$$

where $E_0 \equiv -2\eta \ln[(1-\Delta)/2]$ is a constant.

In summary, the solution to our system of equations in the limit of a small lateral displacement, or equivalently small amplitude, is given by Eq. (12), where the unknown constants in this solution are determined from the boundary conditions, Eqs. (9c), (9d), and (14a), and the equation of state, Eq. (13). The elastic energy of a given solution is determined from Eq. (14b).

A. The flat-to-buckle instability

As a first step of examining the solution we analyze the flat-to-buckle instability; i.e., we assume that the lateral displacement is infinitesimal, and disregard Eq. (14a). Given

the bendo-gases parameter, η, we look for the lowest lateral compression P_x that yields an out-of-plane configuration. The general solution, Eq. (12), together with the linearized form of the boundary conditions, Eqs. (9c) and (9d), and the equation of state, Eq. (13), form a homogenous system of equations for the five unknowns a_i's, P_y, and $P_{\rm ud}$. Nontrivial solutions to these equations exist when their corresponding determinant vanishes. This condition is satisfied when either of the following equations holds:

$$\text{symmetric branch:} \quad \eta \sin u - \frac{u}{3}[(3+u^2)\eta - 6u^4]\cos u = 0, \tag{15a}$$

$$\text{asymmetric branch:} \quad \sin u = 0, \tag{15b}$$

where for simplicity we defined $u \equiv \sqrt{P_x}/2$. The solutions of Eqs. (15a) and (15b) yield respectively the symmetric and asymmetric branches as is further clarified below.

When there is no fluid in the chamber, $\eta = 0$, the smallest lateral compression is given by the symmetric branch at $u = \pi/2$ ($P_x = \pi^2$). This solution coincides with the critical force at which buckling first occurs in the framework of Euler's elastica.

When η is slightly increased, the symmetric branch yet yields the smallest solution for P_x; however, buckling is delayed compared with the classical criterion. Indeed, expanding Eq. (15a) in powers of η gives $P_x \simeq \pi^2 + \frac{64}{\pi^4}\eta$.

At $\eta \equiv \eta^\star = \frac{6\pi^4}{3+\pi^2}$ the solutions of the two branches coincide and satisfy $u = \pi$ ($P_x = 4\pi^2$). This solution is equivalent to the critical force at the second mode of buckling in the framework of Euler's elastica. While for $\eta > \eta^\star$ the solution of the symmetric branch increases, $u \simeq \pi + \frac{(3+\pi^2)^2}{6\pi^3(15+2\pi^2)}(\eta - \eta^\star)$, the solution of the asymmetric branch remains constant. For this reason, when $0 < \eta/\eta^\star < 1$ buckling occurs into the symmetric branch, whereas when $\eta/\eta^\star > 1$ buckling occurs into the asymmetric branch.

B. The height profiles

In this section we further determine the eigenfunctions in each of the two branches, and fix the remaining unknown constant using Eq. (14a); i.e., the lateral displacement is assumed small but not infinitesimal.

1. Symmetric branch

To derive the sheet's configuration in the symmetric branch we first determine the unknown constants a_i and P_y from the solution of the boundary conditions, Eqs. (9c) and (9d). This gives the eigenfunction

$$y(s) = \frac{P_{\rm ud}}{2P_x}(1-s)s + \frac{P_{\rm ud}}{P_x^2}\left[1 - \frac{\cos\left[\sqrt{P_x}(s-1/2)\right]}{\cos(\sqrt{P_x}/2)}\right], \tag{16}$$

where P_x is given by Eq. (15a). This eigenfunction is yet multiplied by the unknown constant, $P_{\rm ud}$. Using Eq. (14a) we find

$$P_{\rm ud} = \frac{16\sqrt{6}u^{7/2}|\cos u|}{\sqrt{6u + 4u(6+u^2)\cos^2 u - 15\sin(2u)}}\Delta^{1/2}, \tag{17}$$

where $u = \sqrt{P_x}/2$.

Given η and Δ, Eqs. (15a), (16), and (17) provide the complete solution of the height profiles in the symmetric branch. Note that, regardless of the values of P_x and $P_{\rm ud}$, this solution is symmetric around the midpoint of the sheet, $s = 1/2$. Note also that when $\eta \to 0$, Eqs. (15a) and (17) reduce to $P_x \simeq \pi^2 + \frac{64}{\pi^4}\eta$ and $P_{\rm ud} \simeq \frac{32}{\pi^2}\sqrt{\Delta}\eta$, and the height function converges to $y(s) \to \sqrt{4\Delta/\pi^2}\sin(\pi s)$, as expected from the first mode of buckling in Euler's elastica.

Last, we calculate the total energy of this branch using Eq. (14b). This gives [36]

$$E_{\rm s} - E_0 = P_x\Delta, \tag{18}$$

where P_x is a solution to Eq. (15a).

2. Asymmetric branch

To derive the height profile of the asymmetric branch we first fix the lateral compression at a constant value, $P_x = 4\pi^2$, in accordance with Eq. (15b). Then, we find the various constants in Eq. (12) from the boundary conditions, Eqs. (9c) and (9d), the equation of state, Eq. (13), and the constraint on the lateral displacement, Eq. (14a). The solution is divided into two regions, depending on the value of η:

$$\eta = \eta^\star: \quad y(s) = \frac{P_{\rm ud}}{16\pi^4}[2\pi^2(1-s)s + 1 - \cos(2\pi s)] + \frac{1}{\pi}\sqrt{\Delta - \frac{15+2\pi^2}{768\pi^6}P_{\rm ud}^2}\sin(2\pi s), \tag{19a}$$

$$\eta > \eta^\star: \quad y(s) = \frac{\sqrt{\Delta}}{\pi}\sin(2\pi s). \tag{19b}$$

While the pressure difference, $P_{\rm ud}$, remains arbitrary in Eq. (19a), and can take any value between $P_{\rm ud} \in [0, P_{\rm ud}^{\rm cr}]$, where

$$P_{\rm ud}^{\rm cr} = \sqrt{\frac{768\pi^6}{15+2\pi^2}}\Delta^{1/2}, \tag{20}$$

it vanishes altogether in the second solution, Eq. (19b), i.e., $P_{\rm ud} = 0$.

Evidently, Eq. (19a) represents a continuous family of solutions that contains as a subset two special configurations: one at $P_{\rm ud} = P_{\rm ud}^{\rm cr}$, where Eq. (19a) coincides with the solution to the symmetric branch, Eq. (16), and the second at $P_{\rm ud} = 0$, where Eq. (19a) coincides with the asymmetric shape, Eq. (19b). Therefore, this set of solutions describes a continuous transformation of the height function from the symmetric branch to the purely asymmetric branch. Note that since the system has a mirror symmetry around the midaxis of the chamber (see discussion at the end of Sec. II), the left-right symmetry in the symmetric branch can be broken in two different directions. One direction, in which the right side of the sheet becomes lower than the left side, is plotted in Fig. 3.

Regardless of the value of η, the total energy of the system in the asymmetric branch is given by

$$E_{\rm as} - E_0 = 4\pi^2\Delta. \tag{21}$$

Therefore, when $\eta = \eta^\star$, the ground state of the energy contains the continuous set of solutions, whereas when $\eta > \eta^\star$ the ground state contains only the second mode of buckling.

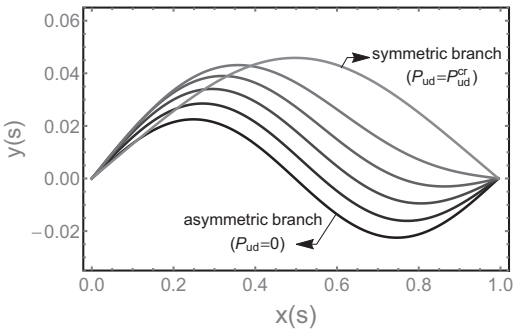

FIG. 3. The continuous family of solutions, Eq. (19a), for $\Delta = 0.005$ and $P_{ud}/P^{cr}_{ud} = \{0, 0.2, 0.4, 0.6, 0.8, 1\}$. Increasing values of the pressure difference are indicated by decreasing intensity of gray. While at $P_{ud} = P^{cr}_{ud}$, Eq. (19a) converges to the height profile of the symmetric branch, Eq. (16) with $P_x = 4\pi^2$; at $P_{ud} = 0$ the solution converges to the second mode of buckling, Eq. (19b). Keep in mind that the system has a mirror symmetry around the midaxis of the chamber. Therefore, an alternative evolution of the system from the symmetric to the asymmetric branch is readily realized when the presented shapes are reflected around the midaxis.

We note that although Eq. (19a) does not possess a strict symmetry, such as the asymmetric profile in Eq. (19b), the name "asymmetric branch" is given to both solutions. This is because they both emanate from the condition in Eq. (15b). Nonetheless, in the forthcoming analysis we refer to the former solution as "asymmetric branch with $P_{ud} \neq 0$," and to the latter solution as "asymmetric solution with $P_{ud} = 0$" (see also the state diagram in Fig. 2).

C. The symmetric-to-asymmetric transition

Our analytical analysis in the small amplitude approximation suggests that the symmetric-to-asymmetric transition is of first order. Indeed, identifying η and P_{ud} as the control and order parameters of the transition, respectively, we find that while the energies of the two branches coincide at $\eta = \eta^\star$, their first derivative, $dE/d\eta$ at $\eta = \eta^\star$, is discontinuous [compare Eqs. (18) and (21)].

Consequently, the order parameter, P_{ud}, experiences a discontinuity at $\eta^\star$. On the one hand, when $\eta \to \eta^\star$ from the left, i.e., from the direction of the symmetric branch, the pressure difference approaches $P_{ud} \to P^{cr}_{ud}$ ($u \to \pi$), where P^{cr}_{ud} is given by Eq. (20). On the other hand, when $\eta \to \eta^\star$ from the right, i.e., from the asymmetric branch, the pressure difference vanishes. Indeed, within this analysis the peculiar behavior encountered at $\eta = \eta^\star$ does not affect the transition at all.

Nonetheless, in the next section we show that when nonlinear effects are taken into consideration, the energetic gap between the symmetric branch at P^{cr}_{ud} and the asymmetric branch with $P_{ud} = 0$ does not vanish, but scales as $\sim\Delta^2$. In addition, when the system evolves within this transition region the elastic profiles that were unstable at the linear order, Eq. (19a), become stable, and allow for a continuous transition between the two branches.

IV. WEAKLY NONLINEAR ANALYSIS: A NUMERICAL INVESTIGATION

In this section we investigate the weakly nonlinear region of the system numerically, i.e., moderate values of the lateral displacement ($\Delta \lesssim 0.1$), and compare the results with the analytical solution obtained at the linear order. The numerical minimization of Eq. (5) is carried out using the conjugate gradient method implemented in MATHEMATICA [37], where the sheet is discretized into $N = 81$ equally spaced points. At a given lateral displacement, Δ, and a vertical dimension of the chamber, $L_y = 1$, we vary the bendo-gases parameter between $\eta/\eta^\star \in [0, 2]$, and at each iteration we record the pressure difference in the chamber and the spatial configuration of the sheet.

The section is divided into three subsections. First, we compare the numerical data with the linear solution. In different from the analytical prediction, we show that the pressure difference changes continuously at the transition between the symmetric branch and the asymmetric branch with $P_{ud} = 0$. Second, we investigate the behavior of the solution close to the transition as a function of the lateral displacement. We obtain scaling laws for the width of the transition region and the energetic gap between the two limiting solutions. Last, based on our numerical analysis we propose a phenomenological solution for the evolution of the pressure difference within the transition region.

A. Comparison with the linear solution

As a first step of examining the solution we fix the lateral displacement at $\Delta = 0.005$, and follow the evolution of the system as a function of η; i.e., we follow the dashed line in Fig. 2. The results of this investigation are plotted in Fig. 4. When $\eta \to 0$ the pressure difference in the chamber vanishes [Fig. 4(a)], and the height profile converges to the first mode of buckling [see the corresponding shape in Fig. 4(b)]. When $\eta = \eta_-$ the pressure difference reaches a maximum value that approximately coincides with the critical pressure at the transition, $P_{ud}(\eta_-) = P^{cr}_{ud}$, where P^{cr}_{ud} is given by Eq. (20). We note that the agreement between $P_{ud}(\eta_-)$ and P^{cr}_{ud} goes beyond the strict limit of the small amplitude approximation and holds even at moderate values of the lateral displacement (see Fig. 5). The elastic profile at this point of a maximum pressure matches the one predicted by the symmetric branch, Eq. (16). We note that despite the relatively large change in the pressure difference, the latter configuration barely changes compared with the first mode of buckling. In between these two limiting cases, $0 < \eta < \eta_-$, the pressure difference increases almost linearly and follows the analytical solution, Eq. (17), derived for the symmetric branch.

When $\eta_- < \eta < \eta_+$ the pressure difference drops rapidly, but yet continuously, to zero. We define η_+ as the point where the pressure difference first vanishes [38]. The elastic profiles in this narrow region coincide with the ones given by the continuous family of solutions, Eq. (19a), which were unstable at the linear order. For example, see point 3 in Fig. 4. Indeed, the continuous variation of the pressure difference across the symmetric-to-asymmetric transition contradicts the pressure

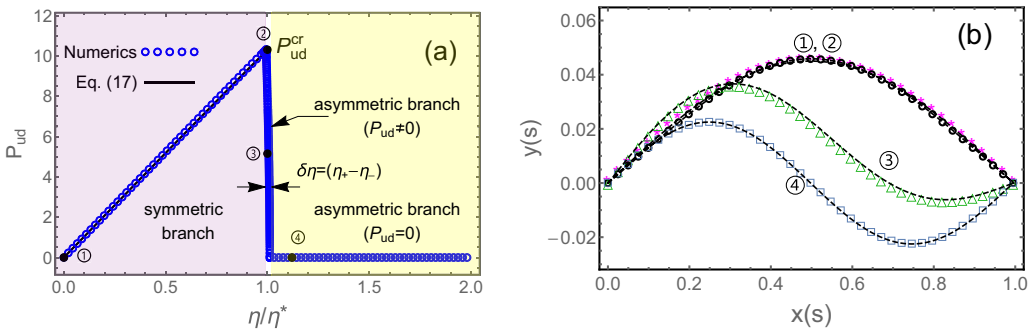

FIG. 4. The evolution of the system when $\Delta = 0.005$. (a) The normalized pressure difference, P_{ud}, is plotted as a function of $\eta/\eta^\star$ and is divided into three regions. One is the symmetric branch (purple shaded area), where the pressure difference follows Eq. (17), and ultimately reaches the critical value P_{ud}^{cr}. The second is a narrow asymmetric branch with $P_{ud} \neq 0$ (white background), marked by $\delta\eta$, in which the pressure difference rapidly drops to zero, and the third is an asymmetric branch with $P_{ud} = 0$ (yellow shaded area). (b) The evolution of the elastic profile. While markers correspond to the numerical profiles, black dashed lines correspond to the analytical solution at the linear order. The profiles labeled by 1 and 2 correspond to the symmetric branch at $P_{ud} = 0$ and $P_{ud} = P_{ud}^{cr}$, respectively [see the corresponding circled numbers in (a)]. The profiles labeled by 3 and 4 correspond respectively to the asymmetric branch with $P_{ud} = P_{ud}^{cr}/2$ [Eq. (19a)] and $P_{ud} = 0$ [Eq. (19b)].

jump predicted by the linear theory. Instead, the transition occurs over a narrow, but yet finite, width of the control parameter, $\delta\eta = \eta_+ - \eta_-$.

Last, beyond the transition region, $\eta > \eta_+$, the pressure difference vanishes and the elastic configuration adopts the second mode of buckling, as given by Eq. (19b).

B. Energy difference and width of the transition region

In this section we further investigate the effect of the lateral displacement on the transition. In particular, we measure how the energetic gap, $\delta E = E_{as}(\eta_+) - E_s(\eta_-)$, and the width over which the transition occurs, $\delta\eta = \eta_+ - \eta_-$, scales with Δ. The results plotted in Fig. 6 reveal these scalings.

While the energetic gap exhibits quadratic dependence on the displacement, $\delta E \simeq c_2\Delta^2$ where $c_2 \simeq 52.0$, the width of the transition region exhibits linear dependence on Δ, i.e., $\delta\eta/\eta^\star \simeq c_1\Delta$, where $c_1 \simeq 3.6$. Consequently, while the energies of the symmetric branch and asymmetric branch with $P_{ud} = 0$ coincide at the linear order, i.e., order Δ, they deviate when nonlinear terms, i.e., order Δ^2, are taken under consideration. Within this energetic gap the asymmetric branch with $P_{ud} \neq 0$ becomes stable. However, its region of stability shrinks to zero as the lateral displacement diminishes.

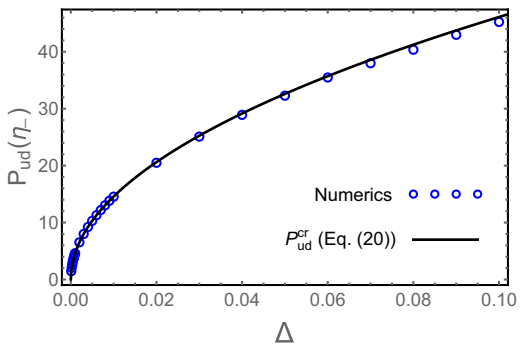

FIG. 5. The maximum pressure difference at $P_{ud}(\eta_-)$ as a function of the lateral displacement. While open blue circles correspond to the numerical values, the solid black line corresponds to the analytical approximation, Eq. (20). Surprisingly, the fit between the analytical and the numerical data goes beyond the strict limit of the small amplitude approximation.

Furthermore, we observe that the boundaries of the intermediate region remain approximately symmetric with respect to $\eta^\star$, i.e., $\eta_\pm/\eta^\star \simeq 1 \pm (c_1/2)\Delta$ [see the inset in Fig. 6(a)]. Deviations from the latter symmetric and linear fit are encountered at large values of Δ. These deviations are most probably due to higher nonlinear contributions to $\delta\eta$ and $\eta_\pm$, e.g., corrections of order Δ^2.

C. The pressure difference profile

Using the preceding results we can approximate the pressure difference within the transition region, $\delta\eta$. Since P_{ud} changes continuously throughout the evolution of the system, the transition from the asymmetric branch with $P_{ud} \neq 0$, Eq. (19a), to the asymmetric branch with $P_{ud} = 0$, Eq. (19b), is of second order. Recalling the universal behavior of supercritical bifurcations, we anticipate a square-root dependence between the order parameter, P_{ud}, and the control parameter, η, close to the transition. Keeping in mind the latter requirements, and that $P_{ud}(\eta_-) \simeq P_{ud}^{cr}$ and $P_{ud}(\eta_+) = 0$, one possible profile of the pressure difference is given by

$$P_{ud} = P_{ud}^{cr}\sqrt{\frac{\eta_+ - \eta}{\eta_+ - \eta_-}}. \tag{22}$$

Note that this relation implies that P_{ud}/P_{ud}^{cr} is independent of Δ. Indeed, substituting $\eta_+ = 1 + c_1\Delta/2$ and $\delta\eta = c_1\Delta$ into Eq. (22), and rescaling the control parameter such that $\eta = 1 + \epsilon$, where $\epsilon = c_1\Delta(1/2 - \tilde{x})$ ($\tilde{x} \in [0, 1]$), gives $P_{ud}/P_{ud}^{cr} = \sqrt{\tilde{x}}$. Yet, as Δ is increased, the width of the transition region, $\delta\eta$, is increased as well, and a subset of solutions within the continuous family of solutions is stretched over a wider region on the η axis. In addition, Eq. (22) suggests that the derivative $dP_{ud}/d\eta$ in the transition region is mildest at $\eta = \eta_-$ and steepest at $\eta \to \eta_+$. Therefore, close to the first critical

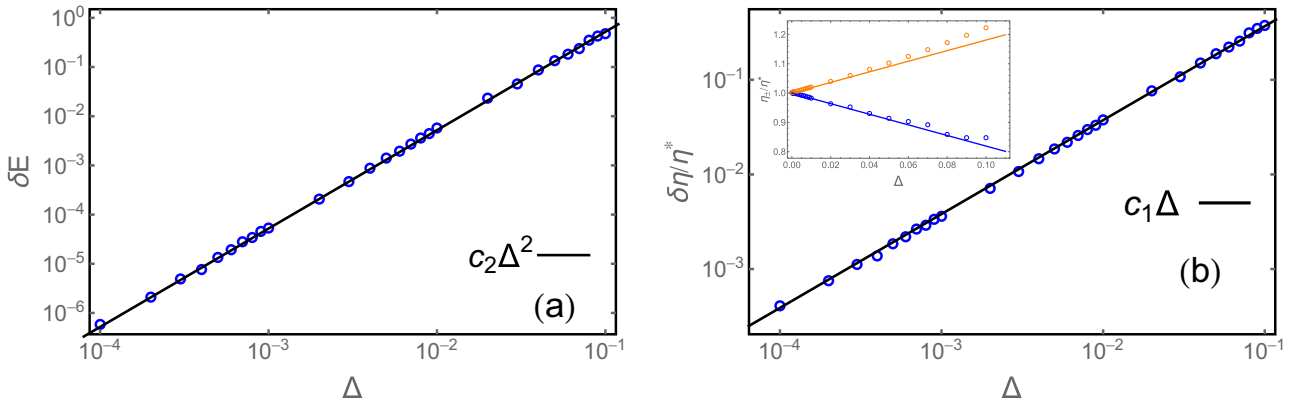

FIG. 6. The energetic gap and the width of the transition region. In both panels logarithmic scales are used on both axes. In addition, open blue circles correspond to the numerical data and solid lines to their corresponding interpolation. (a) The normalized energetic gap, $\delta E = E_{\rm as}(\eta_+) - E_{\rm s}(\eta_-)$, exhibits quadratic dependence on Δ, $c_2 \simeq 52.0$. (b) The normalized width, $\delta\eta = \eta_+ - \eta_-$, exhibits linear dependence on the lateral displacement, where $c_1 \simeq 3.6$. Inset: η_+ (orange) and η_- (blue) are plotted as a function of Δ. The fit to both sets of data is given by $\eta_\pm/\eta^\star \simeq 1 \pm (c_1/2)\Delta$.

transition, i.e., close to $\eta = \eta_-$, solutions at the transition region are easier to access then solutions that are located close to $\eta = \eta_+$.

To verify Eq. (22) numerically we plot the pressure difference as a function of the bendo-gases parameter, $P_{\rm ud}(\eta)$, within the transition region (see Fig. 7). Indeed, we find that data from different lateral displacements all collapse on the same master curve when plotted on the $(\sqrt{(\eta_+ - \eta)/(\eta_+ - \eta_-)}, P_{\rm ud}/P_{\rm ud}^{\rm cr})$ plane.

In summary, the pressure difference exhibits three different solutions as a function of η. One corresponds to the symmetric branch, Eq. (17), the second corresponds to the profile obtained in the narrow transition region, Eq. (22), and the third corresponds to $P_{\rm ud} = 0$ in the purely asymmetric branch.

V. CONCLUSIONS

In this paper we investigated the mutual interaction between a thin sheet and an ideal gas. Our main results are summarized in the state diagram, Fig. 2, that presents three different branches of solutions. Depending on the bendo-gases parameter we showed that asymptotically the system is either governed by the bending energy of the sheet or the energy of the gas. While the former region exhibits a symmetric shape, the latter region favors an asymmetric configuration, which keeps the volumes in the upper and lower parts of the chamber equal.

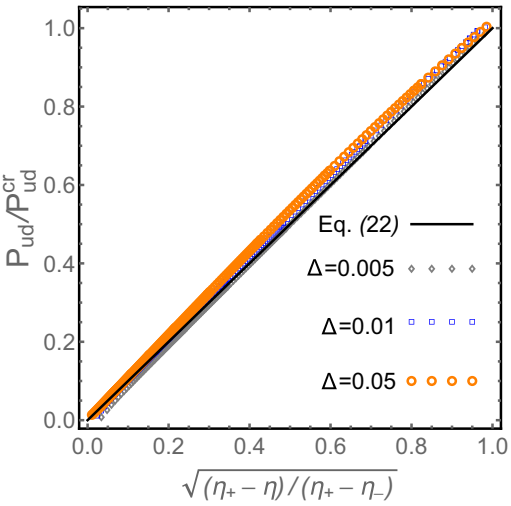

FIG. 7. The normalized pressure difference, $P_{\rm ud}/P_{\rm ud}^{\rm cr}$, as a function of η for several values of the lateral displacement Δ. All data collapse on a single master curve that coincides with the phenomenological profile considered in Eq. (22).

In addition, we investigated the transition between these two limiting scenarios and highlighted a subtle behavior at the leading order of the theory. While the small amplitude approximation yields the three branches of solutions, i.e., the height profiles given in Eqs. (16) and (19), it incorrectly predicts that the asymmetric branch with $P_{\rm ud} \neq 0$, Eq. (19a), is always unstable. Indeed, numerical investigation of the nonlinear formulation revealed that the width over which the latter branch stabilizes is in fact finite. Yet, in the limit of a small lateral compression it remains relatively narrow and scales as $\delta\eta \propto \Delta$. The pressure difference across this region drops rapidly, but yet continuously to zero; i.e., while the linear analysis predicts a discontinuous behavior of the pressure difference at $\eta = \eta^\star$, the addition of nonlinear terms changes the nature of the transition from first to second order. Furthermore, we showed that the energetic gap across the transition region scales as $\sim\Delta^2$; i.e., in this region the system becomes asymptotically soft to variations in the sheet's configuration.

With these observations in mind we were able to estimate the pressure difference throughout the evolution of the system. This main result of our analysis is summarized in the following equation:

$$P_{\rm ud}(\eta, \Delta) = \begin{cases} \text{Eq. (17)}, & \eta \leqslant \eta_- \\ \text{Eq. (22)}, & \eta_- \leqslant \eta \leqslant \eta_+ \\ 0, & \eta \geqslant \eta_+, \end{cases} \tag{23}$$

where $\eta_\pm/\eta^\star \simeq 1 \pm (c_1/2)\Delta$ ($c_1 \simeq 3.6$) are the boundaries of the transition region. While the pressure differences at $\eta \leqslant \eta_-$ and $\eta \geqslant \eta_+$ are predicted by the leading order of the theory, at the transition region, $\eta_- \leqslant \eta \leqslant \eta_+$, it is only estimated phenomenologically, but yet verified by the numerical analysis.

Another direction to control the system, and to investigate its different branches of solutions, is to fix the bendo-gases parameter and then vary the lateral displacement, i.e., follow a vertical line in the state diagram, Fig. 2. This direction is essentially related to the problem of packing a flexible soft object into a small cavity [39–41]. Let us exploit this direction to get some physical intuition regarding the magnitude of the pressure drop that our system can acquire. Consider a chamber with dimensions $L_x = L_y = W = 5$ mm (W is the width) that is divided into two parts by a thin sheet that is made of polyester with Young's modulus $\tilde{E} \simeq 920$ MPa, Poisson's ratio $\nu \simeq 0.3$, and thickness $t = 120$ μm. In addition, assume that the sheet is hinged to the sidewalls of the chamber, and that initially $\Delta = 0$ and $P_u = P_d \simeq 101$ kPa, i.e., $V_u = V_d = L_x L_y W/2$ and atmospheric pressure. Under these conditions, we have that $\eta/\eta^\star \simeq 0.95$, where we used $P_u V_u = N k_B T$, $\eta = P_u V_u L/(WB)$, $B = \tilde{E} t^3/[12(1-\nu^2)]$, and $\eta^\star \simeq 45.4$. Now, suppose that we continuously increase the lateral displacement. Then, we would expect the sheet to evolve within the symmetric branch until η coincides with η_-. Using our approximated solution, $\eta_-/\eta^\star \simeq 1 - (c_1/2)\Delta$, we find that when $\Delta \simeq 0.1$ mm ($L \simeq 5.1$ mm) the system is expected to undergo a transition from the symmetric branch to the asymmetric branch with $P_{ud} \neq 0$. At that point, the pressure drop in the system is approximately given by Eq. (20), i.e., $P_{ud} \simeq 20B/L^3 \simeq 22$ kPa. Had we further increased the lateral displacement the system would have evolved within the intermediate region.

While our study only focused on quasistatic deformations of the sheet, which keep the temperature constant, any experimental realization of the system is expected to exhibit temperature fluctuations, and possibly energy dissipation. In regard to these interesting phenomena we suggest two systems that could be considered in future extensions. First, simulating the ideal fluid as granular gases, composed of macroscopic rigid particles that undergo instantaneous collisions [42,43], could be useful to elucidate the time-dependent temperature variations that take place due to the expansion or compression of the gas. In addition, it would also be interesting to investigate how the velocity distribution function of the gas is correlated with the sheet's trajectory, especially in the transition region, where small variations in the number of particles is expected to yield large changes in the pressure difference. The second extension that could be of interest is a dynamical system that allows the gas to exchange freely between the two sides of the chamber. This system will be useful to elucidate the energetic interplay between the sheet and the fluid during the system's evolution. For example, given the initial and final states of the sheet, one can ask how much of this energy is ultimately converted to displace the fluid from rest. Last, we hope that the study of this system and its dynamic extensions will lay the groundwork for deeper understanding of the interaction between thin sheets and a compressible fluid medium.

ACKNOWLEDGMENTS

We thank D. Serero, H. Diamant, and Y. Feldman for stimulating discussions. We acknowledge financial support from the Pearlstone Center.

[1] S. T. Milner, J. F. Joanny, and P. Pincus, Buckling of Langmuir monolayers, Europhys. Lett. **9**, 495 (1989).
[2] E. Cerda and L. Mahadevan, Geometry and Physics of Wrinkling, Phys. Rev. Lett. **90**, 074302 (2003).
[3] B. Roman and J. Bico, Elasto-capillarity: Deforming an elastic structure with a liquid droplet, J. Phys.: Condens. Matter **22**, 493101 (2010).
[4] H. Diamant and T. A. Witten, Compression Induced Folding of a Sheet: An Integrable System, Phys. Rev. Lett. **107**, 164302 (2011).
[5] A. Fargette, S. Neukirch, and A. Antkowiak, Elastocapillary Snapping: Capillarity Induces Snap-Through Instabilities in Small Elastic Beams, Phys. Rev. Lett. **112**, 137802 (2014).
[6] H. King, R. D. Schroll, B. Davidovitch, and N. Menon, Elastic sheet on a liquid drop reveals wrinkling and crumpling as distinct symmetry-breaking instabilities, Proc. Natl. Acad. Sci. USA **109**, 9716 (2012).
[7] T. J. W. Wagner and D. Vella, Floating Carpets and the Delamination of Elastic Sheets, Phys. Rev. Lett. **107**, 044301 (2011).
[8] F. Box, D. O'Kiely, O. Kodio, M. Inizan, A. A. Castrejón-Pita, and D. Vella, Dynamics of wrinkling in ultrathin elastic sheets, Proc. Natl. Acad. Sci. USA **116**, 20875 (2019).
[9] M. Gomez, D. E. Moulton, and D. Vella, Critical slowing down in purely elastic 'snap-through' instabilities, Nat. Phys. **13**, 142 (2017).
[10] E. Jambon-Puillet, D. Vella, and S. Protière, The compression of a heavy floating elastic film, Soft Matter **12**, 9289 (2016).
[11] O. Oshri, F. Brau, and H. Diamant, Wrinkles and folds in a fluid-supported sheet of finite size, Phys. Rev. E **91**, 052408 (2015).
[12] O. Oshri and H. Diamant, Pattern transitions in a compressible floating elastic sheet, Phys. Chem. Chem. Phys. **19**, 23817 (2017).
[13] L. Pocivavsek, R. Dellsy, A. Kern, S. Johnson, B. Lin, K. Y. C. Lee, and E. Cerda, Stress and fold localization in thin elastic membranes, Science **320**, 912 (2008).
[14] A. Antkowiak, B. Audoly, C. Josserand, S. Neukirch, and M. Rivetti, Instant fabrication and selection of folded structures using drop impact, Proc. Natl. Acad. Sci. USA **108**, 10400 (2011).
[15] J. D. Paulsen, Wrapping liquids, solids, and gases in thin sheets, Annu. Rev. Condens. Matter Phys. **10**, 431 (2019).
[16] B. Davidovitch, R. D. Schroll, D. Vella, M. Adda-Bedia, and E. A. Cerda, Prototypical model for tensional wrinkling in thin sheets, Proc. Natl. Acad. Sci. USA **108**, 18227 (2011).
[17] H. Diamant, Parametric excitation of wrinkles in elastic sheets on elastic and viscoelastic substrates, Eur. Phys. J. E **44**, 78 (2021).
[18] D. P. Holmes, Elasticity and stability of shape-shifting structures, Curr. Opin. Colloid Interface Sci. **40**, 118 (2019).

[19] O. Oshri, Y. Liu, J. Aizenberg, and A. C. Balazs, Delamination of a thin sheet from a soft adhesive winkler substrate, Phys. Rev. E **97**, 062803 (2018).
[20] O. Oshri, Delamination of open cylindrical shells from soft and adhesive Winkler's foundation, Phys. Rev. E **102**, 033001 (2020).
[21] T. Lecuit and P.-F. Lenne, Cell surface mechanics and the control of cell shape, tissue patterns and morphogenesis, Nat. Rev. Mol. Cell Biol. **8**, 633 (2007).
[22] A. Bianco, M. Poukkula, A. Cliffe, J. Mathieu, C. M. Luque, T. A. Fulga, and P. Rørth, Two distinct modes of guidance signalling during collective migration of border cells, Nature (London) **448**, 362 (2007).
[23] R. M. Donlan, Biofilms microbial life on surfaces, Emerging Infect. Dis. **8**, 881 (2002).
[24] J. N. Wilking, T. E. Angelini, A. Seminara, M. P. Brenner, and D. A. Weitz, Biofilms as complex fluids, MRS Bull. **36**, 385 (2011).
[25] J. A. Rogers, T. Someya, and Y. Huang, Materials and mechanics for stretchable electronics, Science **327**, 1603 (2010).
[26] D. Rus and M. T. Tolley, Design, fabrication and control of soft robots, Nature (London) **521**, 467 (2015).
[27] R. Ahmed, F. Mir, and S. Banerjee, A review on energy harvesting approaches for renewable energies from ambient vibrations and acoustic waves using piezoelectricity, Smart Mater. Struct. **26**, 085031 (2017).
[28] L.-Y. Wu, L.-W. Chen, and C.-M. Liu, Acoustic energy harvesting using resonant cavity of a sonic crystal, Appl. Phys. Lett. **95**, 013506 (2009).
[29] W.-C. Wang, L.-Y. Wu, L.-W. Chen, and C.-M. Liu, Acoustic energy harvesting by piezoelectric curved beams in the cavity of a sonic crystal, Smart Mater. Struct. **19**, 045016 (2010).
[30] P. N. Nge, C. I. Rogers, and A. T. Woolley, Advances in microfluidic materials, functions, integration, and applications, Chem. Rev. **113**, 2550 (2013).
[31] S.-H. Chiu and C.-H. Liu, An air-bubble-actuated micropump for on-chip blood transportation, Lab Chip **9**, 1524 (2009).
[32] O. Oshri, Volume-constrained deformation of a thin sheet as a route to harvest elastic energy, Phys. Rev. E **103**, 033001 (2021).
[33] Note that when we retrieve W, the width of the chamber, into the problem the bendo-gases parameter becomes dimensionless, $\eta = Nk_{\mathrm{B}}TL/(WB)$.
[34] A. J. Adams, Postbuckling of circular rings: An analytical solution, J. Math. Phys. **49**, 032902 (2008).
[35] V. M. Vassilev, P. A. Djondjorov, and I. M. Mladenov, Cylindrical equilibrium shapes of fluid membranes, J. Phys. A: Math. Theor. **41**, 435201 (2008).
[36] To derive this energy we substitute the height function, Eq. (16), in the total energy, Eq. (14b), and integrate. Then, we eliminate η and P_{ud} using Eqs. (15a) and (17).
[37] MATHEMATICA, Version 12.0, Wolfram Research, Champaign, IL, 2018.
[38] Numerically, η_+ is determined at the lowest value of η in which the pressure difference drops below $P_{\mathrm{ud}} < 10^{-2}P_{\mathrm{ud}}^{\mathrm{cr}}$. We note that changes by an order of magnitude in this somewhat arbitrary criterion do not affect the final results.
[39] D. J. Schunter, M. Brandenbourger, S. Perriseau, and D. P. Holmes, Elastogranular Mechanics: Buckling, Jamming, and Structure Formation, Phys. Rev. Lett. **120**, 078002 (2018).
[40] D. J. Schunter, R. K. Czech, and D. P. Holmes, Packing transitions in the elastogranular confinement of a slender loop, Soft Matter **16**, 2039 (2020).
[41] N. Stoop, F. K. Wittel, and H. J. Herrmann, Morphological Phases of Crumpled Wire, Phys. Rev. Lett. **101**, 094101 (2008).
[42] S. Chapman and T. G. Cowling, *The Mathematical Theory of Nonuniform Gases*, 3rd ed. (Cambridge University Press, Cambridge, UK, 1970).
[43] N. Sela and I. Goldhirsch, Hydrodynamic equations for rapid flows of smooth inelastic spheres, to Burnett order, J. Fluid Mech. **361**, 41 (1998).